GEOPHYSICS, VOL. 79, NO. 2 (MARCH-APRIL 2014); P. V33–V45, 12 FIGS., 4 TABLES.
10.1190/GEO2013-0170.1

Blind deconvolution of multichannel recordings by linearized inversion in the spectral domain

Michael Behm[1] and Bharath Shekar[2]

ABSTRACT

In seismology, blind deconvolution aims to recover the source wavelet and the Green's function, or parts of it (e.g., reflectivity series), from a recorded seismic trace. A multitude of algorithms exist that tackle this ill-posed problem by different approaches. Making assumptions on the phase spectra of the source wavelet and/or the statistical distribution of the reflectivity series is useful for single trace. The nature of closely spaced multichannel recordings enables a better estimation of a common source wavelet and thus increases the confidence of the results. This approach has been exploited in the past, although different types of assumptions are used for a variety of algorithms. We introduced a new method for simultaneous reconstruction of arbitrary source wavelets and local vertical reflectivity series from teleseismic earthquakes. Closely spaced receivers record vertically incident earthquake body waves and their surface-related multiples, which comprise the unknown reflectivity series. By assuming a common source wavelet for all receivers, the observation of several events resulted in a set of convolution equations relating the unknown source wavelets and unknown reflectivity series to the observed seismic trace. The overdetermined system of equations was linearized and solved by conventional inversion algorithms in the spectral domain. Synthetic tests indicated a better performance of the introduced method than conventional deconvolution in the presence of white noise, which is attributed to the constraint of a common model for all observations. Application to field data from a local deployment allowed imaging a basement reflector from teleseismic body waves, although the data were contaminated with strong coherent noise. From a practical point of view, the presented method is potentially well suited for local and regional large-scale imaging from multichannel passive seismic data.

INTRODUCTION

Blind deconvolution is a term coined in signal processing theory and aims at reconstructing the unknown source wavelet $w(t)$ and the unknown transfer function $r(t)$ from the observed convolution $z(t) = r(t) * w(t)$. It is obvious that assumptions on either $w(t)$, $r(t)$, or both, have to be made to derive a solution. Conventional deconvolution might be regarded as a special case of blind deconvolution because an estimate of $w(t)$ can be obtained from the autocorrelation of $z(t)$ in case $r(t)$ is white. Because the autocorrelation provides the amplitude spectra only, premises on the phase spectrum of $w(t)$ (e.g., minimum phase) have to be made. Wiggins (1978) introduces the minimum entropy deconvolution method based on kurtosis maximization of the transfer function. Minimum entropy deconvolution does not rely on the minimum-phase assumption, but it requires a broadband source wavelet. To circumvent the broadband precondition, advanced statistical approaches have emerged in the field of electrical engineering (e.g., Cadzow and Li, 1995) as well as in seismic exploration (e.g., van der Baan and Pham, 2008). In earthquake seismology, multichannel recordings are often used to obtain an estimate of the source wavelet by averaging the recordings. If the source wavelet of an earthquake is stationary with respect to the receiver array aperture, the average wavelet of all receivers can be deconvolved from the individual recordings to obtain $r(t)$. This method is used to image lateral subsurface variations on basin scale (e.g., Yang et al., 2012) and on crustal scale (e.g., Tseng and Chen, 2006). Simultaneous least-squares deconvolution of several seismic events (Gurrola et al., 1995) is an

Manuscript received by the Editor 1 May 2013; revised manuscript received 18 September 2013; published online 17 February 2014.
[1]Colorado School of Mines, Department of Geophysics, Golden, Colorado, USA and University of Vienna, Department for Meteorology and Geophysics, Vienna, Austria. E-mail: michael.behm@univie.ac.at.
[2]Colorado School of Mines, Department of Geophysics, Golden, Colorado, USA. Email: bshekar@mines.edu.

alternative approach. Based on the theory of homomorphic systems, multichannel recordings can be transformed into the log-spectral domain where averaging leads to an improved estimate of the source wavelet (Otis and Smith, 1977). This approach has been used in exploration seismology (Tria et al., 2007) as well as in earthquake seismology (Bostock and Sacchi, 1997). The latter study makes uses of multisource and multichannel recordings to sharpen later teleseismic arrivals (e.g., reflections from the mantle-core boundary). Bostock (2004) revisits these concepts in a more elaborate framework, which includes the evaluation of 3C recordings to get more insight into the crustal structure on the receiver side. From a practical point of view, many of the aforementioned studies focus on the reconstruction of the source wavelet in the spectral (or log-spectral) domain, which in turn is deconvolved from the data. In contrast, Kaaresen and Taxt (1998) introduce a method for multichannel data and sparse reflectivity, which estimates $w(t)$ and $r(t)$ by a quasisimultaneous, iterative scheme in the time domain.

Although by far not exhaustive, the list of cited studies illustrates that blind deconvolution finds its application in exploration and earthquake seismology. Bridging the gap between these two fields is further facilitated by the industry's growing attention for passive seismology and broadband data. In particular, the interest in the low-frequency spectrum of seismic data is mainly driven by the need for robust initial velocity models for full-waveform inversion (Sirgue and Pratt, 2004; Denes et al., 2009). Passive seismology is well suited to provide those low frequency data (e.g., <10 Hz) due to the instrument specifications and the wide range of possible sources (e.g., cultural noise and regional and global seismicity). Passive seismic methods might also be used to get a large-scale image of unexplored terrain without using active sources (Leahy et al., 2012; Behm et al., 2013; Biryol et al., 2013). We introduce a new blind deconvolution method for imaging local vertical reflectivity series from teleseismic events which were recorded on a passive array in southwestern Wyoming. The data were acquired in academia-industry cooperation to investigate the feasibility of passive seismology for large-scale subsurface characterization. Therefore, the presented study also aims to contribute to the aforementioned topics.

As it is outlined in the next section, our approach might also be seen in the context of seismic interferometry (e.g., Schuster, 2010; Wapenaar et al., 2010). Quoting Galetti and Curtis (2012), "seismic interferometry refers to a range of methods by which seismograms are constructed by correlation of other wavefields." Seismic interferometry has proven to be very successful in retrieving surface waves from ambient noise on global, regional, and local scales, with overviews given by Bensen et al. (2007) and Behm et al. (2013). Forghani and Snieder (2010) outline why it is more difficult to retrieve body waves and thus the reflectivity structure from noise interferometry. Nonetheless, several studies demonstrate the applicability for obtaining reflections from interferometry. Draganov et al. (2009) investigate a local deployment in Libya and retrieve shallow reflectors from road noise. Ruigrok et al. (2010) use different phases from nonvertical incidence teleseismic earthquakes to image the reflectivity structure down to depths of 60 km below the Cheyenne belt in Wyoming. They use processing routines from reflection seismology (semblance analysis, migration, etc.) and finally derive images with improved resolution compared to receiver function (RF) analysis. The RF analysis method is commonly used to map crustal structure from converted body waves. Galetti and Curtis (2012) illustrate that seismic interferometry can be thought of as a generalization of RF analysis. They relate their findings also to the pioneering work of Claerbout (1968) who shows that the autocorrelation of recorded ambient noise at a receiver can be used to derive the reflection response at the same location. Edme and Halliday (2012) introduce iterative gapped spiking deconvolution to ambient noise recordings and derive improved images compared to autocorrelation.

METHOD

A set of N seismic events is recorded on an array comprising M receivers. Those receivers are closely spaced, such that the source wavelet $w_n(t)$ of each event is invariant with respect to the receiver location. It is further assumed that the incoming wave is a vertically incident plane wave. Although the latter constraint is satisfied by teleseismic events with epicentral distances greater than 30°, in the case of a small array aperture (<100 km), the validity of the wavelet invariance assumption mainly depends on two factors. These are the size of the Fresnel zone and the size and magnitude of the impedance discontinuities along the raypath between the source location and the maximum imaging depth at the receiver side. If the spatial extent of these velocity discontinuities is large in comparison to the array aperture, the source wavelets at each individual station are affected by the same transmission coefficients and are identical at each receiver. The local vertical reflectivity series at each receiver station is denoted by $r_m(t)$, and the duration of $r_m(t)$ corresponds to the aforementioned maximum possible imaging depth. The observed seismic trace $z_{nm}(t)$ is associated with the nth event recorded at station m. It is modeled by the superposition of the incoming wave $w_n(t)$ and its convolution with $r_m(t)$ after the reflection at the free surface (Figure 1a):

$$\begin{aligned} z_{nm}(t) &= s(w_n, r_m, t) + \mathrm{noise}(t) \\ &= w_n(t) - r_m(t) * w_n(t) + \mathrm{noise}(t). \end{aligned} \tag{1}$$

In equation 1, the star sign denotes convolution. Taking the superposition of the wavelet and the convolution term instead of convolution only is of crucial importance when the duration of the wavelet is equal or larger than the zero-offset two-way traveltimes of the expected reflections (or in other words, when the weaker reflectivity responses are buried beneath the strong source wavelet; Figure 1b). The negative sign of the convolution term in equation 1 results from the reflection coefficient at the free surface (−1) and the desire for using the convention nomenclature for reflectivity, in which positive impedance contrasts are described by positive reflection coefficients. Although all statements so far have been made with P-waves or pressure in mind, they are also valid for S-waves where the free surface reflection coefficient is +1, and positive impedance contrasts are characterized by negative reflection coefficients (Aki and Richards, 2009). It should be noted that $w(t)$ does not represent the exact source-time function of the earthquake because it is imprinted by all transmission coefficients between the source and the receiver surface side. We also emphasize that equation 1 is a linearization because it does not take higher-order receiver-side multiples into account, and the effect of this simplification is analyzed in synthetic tests in the next section.

To strictly fulfill the aforementioned invariance assumption for the source wavelet, it is further required that the product of the transmission coefficients between the imaging depth and the receiver surface is constant over all receivers. This is guaranteed if the targeted discontinuities extend throughout the imaging area, and if the impedance contrast is constant along the discontinuities. Again, this is taken for granted if the array aperture is small. We use the surface as a mirror, and by that we aim to recover a transfer function (the vertical reflectivity series) below each station from the correlation (deconvolution) of the recording with itself. Each receiver also acts as a virtual source (Bakulin and Calvert, 2006), and our approach can also be classified into the group of seismic interferometric methods (e.g., Schuster, 2010; Wapenaar et al., 2010). Deviation from the vertical-incidence assumption has two consequences. First, the stationary phase assumption (Snieder, 2004) of seismic interferometry is violated. Translated to ray theory, the stationary phase assumption implies that the raypath of the waves, which are correlated (deconvolved) to gain the transfer function between two stations (the virtual source and the receiver), must be identical prior their arrival to any of the two stations. If we want to recover the vertical reflectivity series below a single station, which acts simultaneously as a virtual source and receiver, this condition is only met for vertical incidence and horizontal layering (Figure 1c and 1d). The second consequence is related to the combination of the depth of a reflector and the frequency content of the data. The typical range of horizontal slowness for teleseismic P-waves ranges between 0.04 s/km (~100° epicentral distance) and 0.08 s/km (~30° epicentral distance). These values correspond to angles of incidence of almost 30° to 14° for a typical crustal velocity of approximately 6 km/s. The differences in two-way arrival times due to the varying inclination of the rays depend on the depth of the reflector and can be in the range of 0.5–2.0 s for deeper crustal features (e.g., the Moho). The frequency content of teleseismic P-waves used in this study peaks at approximately 0.5–1.0 Hz. Thus, it may appear that reflections from deeper crustal structures suffer from destructive interference if a broad range of epicentral distances and back azimuths is used. We address the deviation of the vertical incidence assumption as well as the deviation from strict horizontal and continuous layering by a synthetic test in the next section.

In the spectral domain, equation 1 becomes the complex-valued equation:

$$\begin{aligned} Z_{nm}(f) &= S(W_n, R_m, f) + \text{noise}(f) \\ &= W_n(f) - R_m(f) \cdot W_n(f) + \text{noise}(f). \end{aligned} \tag{2a}$$

In the following, the argument (f) is dropped from the notation for simplicity. The function $S(W_n, R_m)$ in equation 2a is explicitly rewritten in terms of real and imaginary parts:

$$S^R(W_n, R_m) = W_n^R - W_n^R \cdot R_m^R + W_n^I \cdot R_m^I, \tag{2b}$$

$$S^I(W_n, R_m) = W_n^I - W_n^R \cdot R_m^I - W_n^I \cdot R_m^R, \tag{2c}$$

where the superscripts R and I indicate real and imaginary parts, respectively. If the noise is neglected, $2 \times (N \times M)$ observations (Z_{nm}^R, Z_{nm}^I) and $2 \times (N + M)$ unknowns $(W_n^R, W_n^I, R_m^R, R_m^I)$ are derived for each frequency component (f). If either N or M is greater than 2, the equation system is overdetermined and is solved by linearization with respect to the unknowns (e.g., Rawlinson and Sambridge, 1998). Starting from an initial model $(W_{n0}^R, W_{n0}^I, R_{m0}^R, R_{m0}^I)$, the linearization is described by

$$\Delta S_{nm}^R = Z_{nm}^R - S^R(W_{n0}^R, W_{n0}^I, R_{m0}^R, R_{m0}^I), \tag{3a}$$

$$\Delta S_{nm}^I = Z_{nm}^I - S^I(W_{n0}^R, W_{n0}^I, R_{m0}^R, R_{m0}^I), \tag{3b}$$

$$\begin{aligned} \Delta S_{nm}^R = {} & \frac{\partial S^R}{\partial W_n^R} \cdot \Delta W_n^R + \frac{\partial S^R}{\partial W_n^I} \cdot \Delta W_n^I + \frac{\partial S^R}{\partial R_m^R} \cdot \Delta R_m^R \\ & + \frac{\partial S^R}{\partial R_m^I} \cdot \Delta R_m^I + \text{noise}^R, \end{aligned} \tag{3c}$$

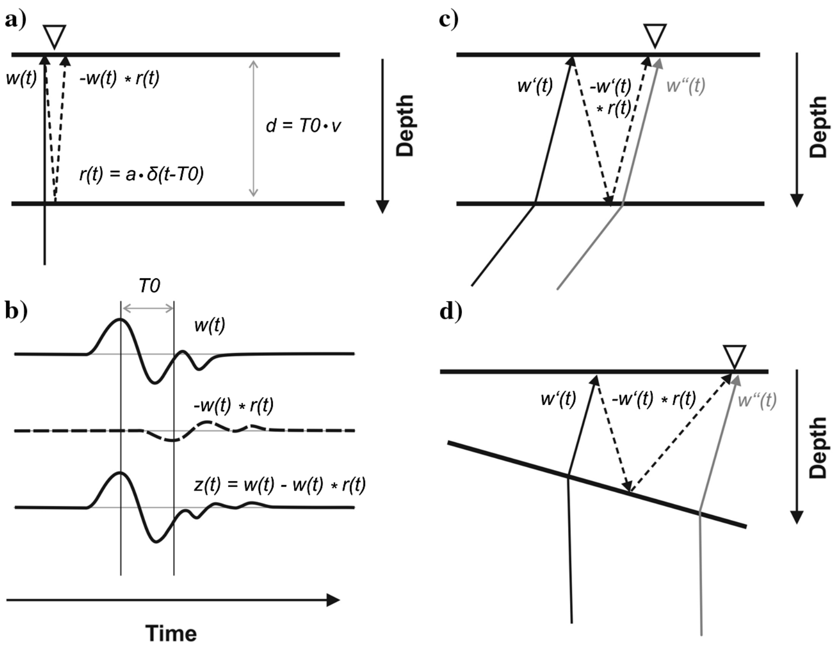

Figure 1. (a) Superposition of a low-frequency vertically incident plain wave $w(t)$ and its convolution with the near-surface reflectivity series $r(t)$ after the reflection at the free surface. (b) The relatively weak reflection in the recording $z(t)$ at time $T0$ is hidden by the stronger source wavelet: v, velocity above the reflector; d, $T0$, a, depth, two-way traveltime, and reflection coefficient of the reflector; and δ, Delta-function. The star sign denotes convolution. Violation of the stationary phase principle due to (c) nonvertical incidence and (d) vertical incidence and inclined reflectors: $w''(t)$ and $w'(t)$ have different paths and are imprinted by different transmission series above the reflector.

$$\Delta S^I_{nm} = \frac{\partial S^I}{\partial W^R_n} \cdot \Delta W^R_n + \frac{\partial S^I}{\partial W^I_n} \cdot \Delta W^I_n + \frac{\partial S^I}{\partial R^R_m} \cdot \Delta R^R_m + \frac{\partial S^I}{\partial R^I_m} \cdot \Delta R^I_m + \text{noise}^I. \tag{3d}$$

Note that the noise is now regarded as the part of the data Z_{mm} that cannot be fitted by the model S. The partial derivatives in equations 3c and 3d are given by

$$\frac{\partial S^R}{\partial W^R_n} = 1 - R^R_m, \tag{4a}$$

$$\frac{\partial S^R}{\partial W^I_n} = R^I_m, \tag{4b}$$

$$\frac{\partial S^R}{\partial R^R_m} = -W^R_n, \tag{4c}$$

$$\frac{\partial S^R}{\partial R^I_m} = W^I_n, \tag{4d}$$

$$\frac{\partial S^I}{\partial W^R_n} = -R^I_m, \tag{4e}$$

$$\frac{\partial S^I}{\partial W^I_n} = 1 - R^R_m, \tag{4f}$$

$$\frac{\partial S^I}{\partial R^R_m} = -W^I_n, \text{ and} \tag{4g}$$

$$\frac{\partial S^I}{\partial R^I_m} = -W^R_n. \tag{4h}$$

Adopting a conventional nomenclature, these linearized equations are formulated in matrix notation as

$$\mathbf{B} \cdot \mathbf{x} = \mathbf{y}, \tag{5}$$

where $\mathbf{x}$ is the vector of model parameter updates (ΔW^R_n, $\Delta W^I_n, \Delta R^R_m, \Delta R^I_m$), $\mathbf{y}$ comprises the reduced observations (ΔS^R_{nm}, ΔS^I_{nm}; equations 3a and 3b), and $\mathbf{B}$ contains the partial derivatives (equations 4a–4h). Both $\mathbf{y}$ and $\mathbf{B}$ are evaluated at the initial model ($W^R_{n0}, W^I_{n0}, R^R_{m0}, R^I_{m0}$). Continuity constraints on the reflectivity series ($\mathbf{C}$, $\boldsymbol{\Delta\varphi}$, $\boldsymbol{\Delta\tau}$; see below) are appended in the form of additional rows to $\mathbf{B}$ and $\mathbf{y}$, such that equation 5 becomes

$$\begin{bmatrix} \mathbf{B} \\ \mathbf{C} \end{bmatrix} \cdot \mathbf{x} = \begin{bmatrix} \mathbf{y} \\ -\boldsymbol{\Delta\tau} \\ -\boldsymbol{\Delta\varphi} \end{bmatrix} = \mathbf{D} \cdot \mathbf{x} = \mathbf{y}'. \tag{6}$$

Equation 6 is solved for $\mathbf{x}$ by the least-squares solution:

$$\mathbf{x} = (\mathbf{D^T} \cdot \mathbf{D})^{-1} \cdot \mathbf{D^T} \cdot \mathbf{y}'. \tag{7}$$

Although $\mathbf{D^T} \cdot \mathbf{D}$ is overdetermined, the inverse in equation 7 may be ill posed and is calculated by spectral decomposition. By allowing only large singular values and corresponding singular vectors to contribute to the solution, spectral decomposition minimizes the projection of noise on the model in case of poorly conditioned systems. A small condition number of the equation system 7 (linear dependence of the rows in $\mathbf{B}$ and $\mathbf{y}$) can be due to source wavelets having similar signatures. This might occur when rupture processes in a localized region are of identical or similar characteristics and magnitude. In practice, this possible pitfall can be avoided by checking the source wavelets and/or the condition number prior to inversion. The columns of $\mathbf{B}$ are weighted to account for a possible numerical discrepancy between the source amplitude spectra and the reflectivity series spectra. Additionally, manually chosen weighting factors are introduced to determine the relative importance of source wavelets and reflectivity series. Due to the nonlinearity in equation 2, the updates are damped by a factor β (<1) prior to their addition to the initial model:

$$\begin{bmatrix} \mathbf{w}^R \\ \mathbf{w}^I \\ \mathbf{r}^R \\ \mathbf{r}^I \end{bmatrix} = \begin{bmatrix} \mathbf{w}^R_0 \\ \mathbf{w}^I_0 \\ \mathbf{w}^R_0 \\ \mathbf{w}^I_0 \end{bmatrix} + \beta \cdot \mathbf{x}. \tag{8}$$

In equation 8, ($\mathbf{w}^R$, $\mathbf{w}^I$, $\mathbf{r}^R$, and $\mathbf{r}^I$) are column vectors comprising the Fourier coefficients of all source wavelets and reflectivity series for a single frequency component. The choice of β depends on the data. Finally, the initial model is replaced by the updated model, and the entire procedure is iterated starting from equations 3a–3d until convergence is achieved.

Stabilization of inversion is achieved by adding additional constraints on the model parameters. For example, asking for a smooth model by setting the second spatial derivative of the velocity to zero is common practice in traveltime tomography and full-waveform inversion. The model parameters in this study are the spectra of source wavelets and reflectivity series, and the inversion is performed independently for each frequency component. With respect to the assumptions on the method, lateral continuity along a reflector is regarded as a more useful constraint than its smoothness. Lateral continuity is expressed by setting the difference of the reflectivity series between adjacent stations to zero. For each station pair, two continuity constraints for the real and imaginary parts of the Fourier coefficients ($\mathbf{r}^R$, $\mathbf{r}^I$) are derived. It is reasonable to treat amplitude spectra and phase spectra independently because the first one represents the reflection coefficient and the latter one the associated two-way traveltime of a reflector. By expressing the amplitude τ and the phase φ through the unknowns (real and imaginary parts), the continuity equations between two stations (A and B) are formulated by

$$\Delta\tau_{AB} = \tau_A - \tau_B = \sqrt{(R^R_A + R^I_A)^2} - \sqrt{(R^R_B + R^I_B)^2} = 0, \tag{9a}$$

$$\Delta\varphi_{AB} = \varphi_A - \varphi_B = \tan^{-1}\left(\frac{R_B^I}{R_B^R}\right) - \tan^{-1}\left(\frac{R_A^I}{R_A^R}\right) = 0. \quad (9b)$$

The indices (A and B) are replaced by the corresponding m, and M stations result in $M \times (M-1)$ independent continuity equations 9a and 9b. Their linearization leads to the matrix formulation:

$$\mathbf{C} \cdot \mathbf{x} = \begin{bmatrix} -\Delta\boldsymbol{\tau} \\ -\Delta\boldsymbol{\varphi} \end{bmatrix}. \quad (10)$$

Note that $\mathbf{x}$ in equation 10 contains the real and imaginary parts of the reflectivity series (ΔR_m^R, ΔR_m^I) only, but not the source wavelets as in equation 5. The partial derivatives in $\mathbf{C}$ calculate as

$$\frac{\partial\Delta\tau_{AB}}{\partial R_A^R} = \frac{R_A^R}{\tau_A}, \quad (11a)$$

$$\frac{\partial\Delta\tau_{AB}}{\partial R_A^I} = \frac{R_A^I}{\tau_A}, \quad (11b)$$

$$\frac{\partial\Delta\tau_{AB}}{\partial R_B^R} = \frac{-R_B^R}{\tau_B}, \quad (11c)$$

$$\frac{\partial\Delta\tau_{AB}}{\partial R_B^I} = \frac{-R_B^I}{\tau_B}, \quad (11d)$$

$$\frac{\partial\Delta\varphi_{AB}}{\partial R_A^R} = \frac{-R_A^I}{\tau_A}, \quad (11e)$$

$$\frac{\partial\Delta\varphi_{AB}}{\partial R_A^I} = \frac{R_A^R}{\tau_A}, \quad (11f)$$

$$\frac{\partial\Delta\varphi_{AB}}{\partial R_B^R} = \frac{-R_B^I}{\tau_B}, \quad (11g)$$

$$\frac{\partial\Delta\varphi_{AB}}{\partial R_B^I} = \frac{-R_B^R}{\tau_B}. \quad (11h)$$

The coefficients of $\mathbf{C}$ and the misfits ($\Delta\boldsymbol{\tau}$ and $\Delta\boldsymbol{\varphi}$) are evaluated at each iteration step. The rows of $\mathbf{C}$ are individually weighted by their interstation distance, and manually chosen weights control the relative importance of amplitude continuity versus phase continuity. After padding the source wavelets columns in $\mathbf{C}$ and the source wavelet rows of $\mathbf{x}$ with zeros, equation 10 is appended to $\mathbf{B}$ and $\mathbf{y}$ prior to the calculation of the inverse (equations 5 and 6).

SYNTHETIC TESTS

The applicability of the outlined methodology is tested on synthetic data sets. A 2D reflectivity model is based on the expected subsurface structure of the region where the field data (next section) were acquired (Gans, 2011; Leahy et al., 2012). It comprises a 9-km-long section with five distinct layers (Figure 2, Table 1). With the exception of the low-angle fault, which separates layer 1 from layer 2, all interfaces are horizontal. Transmission and reflection coefficients between the layers are calculated for vertically incident P-waves (Aki and Richards, 2009) and are summarized in Table 2.

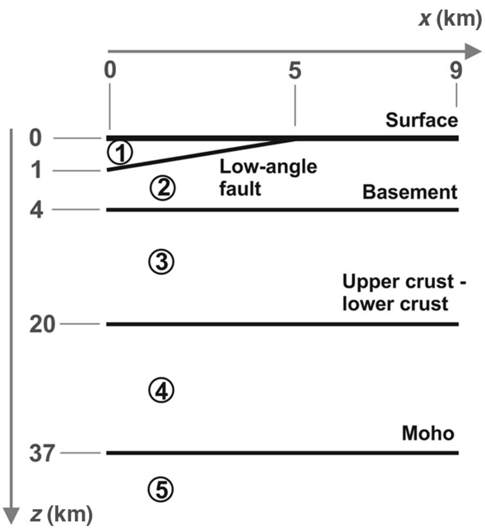

Figure 2. Schematic of the subsurface model used for calculation of synthetic reflectivity data (not to scale). Encircled numbers refer to the layers in Table 1.

Table 1. Parameters used for the synthetic model (Figure 2).

Layer	Description	Upper/lower interface	V_P (km/s)	V_S (km/s)	Density (g/ccm)	Vertical extent (top/bottom) (km)
1	High-velocity layer (carbonates)	Surface/low-angle fault	5.0	2.50	2.50	0/1–0
2	Sediment (shale)	Surface/low-angle fault — basement	4.0	1.96	2.30	1–0/4
3	Upper crust (granite)	Basement/crustal interface	6.3	3.70	2.80	4/20
4	Lower crust	Crustal interface/Moho	6.5	3.71	2.85	20/37
5	Mantle	Moho	8.0	4.45	3.30	37

Fifty-five receivers are distributed along the 9-km-long section. For each receiver, a reflectivity model $r(t)$ is obtained by multiplication of the corresponding reflection and transmission coefficients for the down- and upgoing waves and conversion to vertical two-way traveltimes. These total reflectivity coefficients calculate as −0.15, 0.30, 0.02, and 0.16 for the low-angle fault, the basement, the upper/lower crust boundary, and the Moho at the left side of the section where the low-angle fault is present. The corresponding numbers at the right side, where the low-angle fault does not exist, are almost identical (0.31, 0.02, and 0.16 for the basement, the upper/lower crust boundary, and the Moho). Five source wavelets $w(t)$ are calculated by applying different Butterworth filters to a spike (Ryan, 1994). The Butterworth filter is chosen for its flexibility in creating minimum- and mixed-phase spectra, which also characterize real earthquake wavelets. The used frequency content ranges from 0.3 to 1.8 Hz. Those values are selected based on the real data set (see next section). Synthetic observation data $z(t)$ are calculated for each wavelet by evaluating equation 1. White noise is added to $z(t)$ in the frequency range 0.2–2.0 Hz, in which the signal-to-noise ratio (S/N) is specified as the ratio of the maximum absolute amplitude of $w(t)$ to the maximum range of the uniform noise distribution. The used wavelets and examples of synthetic data are shown in Figure 3. The synthetic data illustrate the two major challenges that are (1) the burial of shallow reflections beneath the source wavelet and (2) the weak reflection signatures in the presence of noise. If the source wavelet is of a more complex shape (e.g., wavelet no. 2), these difficulties aggravated.

A multitude of inversions of this synthetic data set is performed to get a better understanding of the inversion parameters. Five source wavelets and 55 stations result in 275 observed traces versus 60 unknown source wavelets and reflectivity series. The exact onset of a wavelet is sometimes difficult to define on real data, but it does not need to be known because the phase spectra are part of the solution. The initial reflectivity is zero at all stations, and each initial source wavelet $w_n(t)$ is calculated as the average of the first 6 s of all corresponding receiver recordings $z_{nm}(t)$. Apart from noise-free data, two additional data sets with S/N of 2.0 and 1.0 dB, respectively, are also inverted. For comparison, conventional single-trace deconvolution followed by stacking over all events is also applied to the data. The estimated source wavelets for deconvolution are identical to the initial source wavelets described afore. In the following, we summarize the most important findings of the synthetic test.

The number of used singular values and singular vectors depends on the S/N, but also on the weight of the continuity constraints. In most inversions, the damping factor β (equation 8) must be kept small (0.1–0.2) to guarantee stability, which indicates a strong degree of nonlinearity. Accordingly, a large number of iterations (30–50) are necessary to achieve convergence. A crucial parameter is the relative weight of the source wavelet and the reflectivity series (Figure 4). Although the effect of strong versus weak weighting has not much effect on the estimation of the source wavelet itself (Figure 4d and 4e), there is a pronounced difference in the obtained reflectivity series (Figure 4a and 4b). The overall ringing character of the reflectivity solution shown in Figure 4b possibly expresses a compensation for spurious small amplitudes in the corresponding source wavelet solution (Figure 4e). On the other hand, only the result from strong source wavelet weighting (Figure 4b) indicates the reflection from the low-angle fault. Thus, there is no obvious best choice for this parameter, and we take this as another expression of strong nonlinearity. The true, initial, and obtained source wavelets are very similar in general, which possibly results from the strong amplitude of the incoming wave in comparison to the reflected waves. Conventional deconvolution applied to the noise-free data set (Figure 4c) provides a result similar to blind deconvolution with weak source wavelet weighting (Figure 4a). However, more artifacts appear in the uppermost section (0–1 s) because deconvolution does not take the superposition of the incoming and reflected waves into account. The weak reflectivity contrast at the upper/lower crust boundary is not resolved adequately with any of the methods. It is also noted that the polarity of the reflectors is correctly reconstructed.

Figure 5 illustrates results from the inversion of the data set with an S/N of 1 dB. There is a clear improvement when the continuity constraints are enforced (Figure 5b versus 5a). Conversely, conventional deconvolution (Figure 5c) performs poorly in reconstructing the reflectivity

Table 2. Vertical incidence reflection/transmission coefficients for reflection and transmission between the layers of the synthetic model (Figure 2, Table 1).

Reflection/transmission	From layer 1	From layer 2	From layer 3	From layer 4	From layer 5
To layer 1	—	0.15/0.85	—	—	—
To layer 2	−0.15/1.15	—	−0.31/1.31	—	—
To layer 3	—	0.31/0.69	—	−0.02/1.02	—
To layer 4	—	—	0.02/0.98	—	−0.18/1.18
To layer 5	—	—	—	0.18/0.82	—

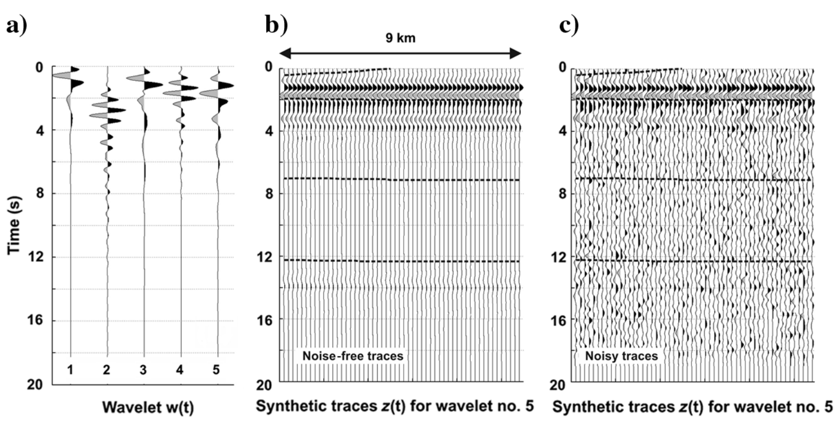

Figure 3. (a) Five different mixed-phase source wavelets which are used for the synthetic test. (b and c) Synthetic data for injecting source wavelet no. 5 into the model shown in Figure 2. Dashed lines indicate the vertical two-way traveltimes associated with the reflectors (fault, basement, upper/lower crust boundary, and Moho). The S/N in (c) is 1.

series. The low-angle fault is not recovered in any of the inversions nor with conventional deconvolution. A second suite of tests was run on synthetic data sets based on more complicated source wavelets (e.g., longer coda). As expected, the recovery of the reflectivity structure degrades with the complexity of the source wavelets, in particular in combination with a low S/N. In this case, the continuity constraints become more important, and blind deconvolution performs far superior to standard deconvolution.

The above tests target primarily the validity and performance of the algorithm and its implementation. As outlined in the previous

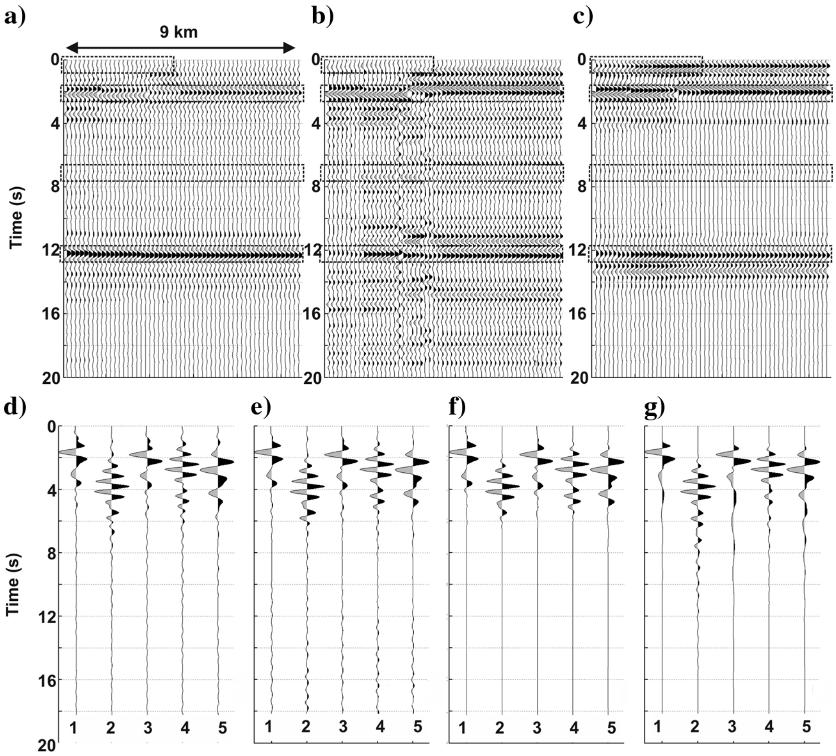

Figure 4. Estimated reflectivity time series and source wavelets from noise-free synthetic data: Reflectivity series (a) and source wavelets (d) for weak (0.1) relative source wavelet weighting. Reflectivity series (b) and source wavelets (e) for strong (1.0) relative source wavelet weighting. Note the spurious amplitudes at later times ($T > 12$ s) in (e). (c) Reflectivity series obtained by deconvolution. The polarity is plotted reverse because deconvolution with the source wavelet does not take the reflection coefficient (−1) at the free surface into account. (f) Initial source wavelets for inversion and deconvolution. (g) True source wavelet used for generation of synthetic data. All traces are band-pass filtered in the range of 0.5–2.0 Hz. The dashed rectangles are centered at the vertical two-way traveltimes associated with the reflectors in the synthetic model. The ringing character of the blind deconvolution and conventional deconvolution reflectivity series results from the band-limited frequency spectrum.

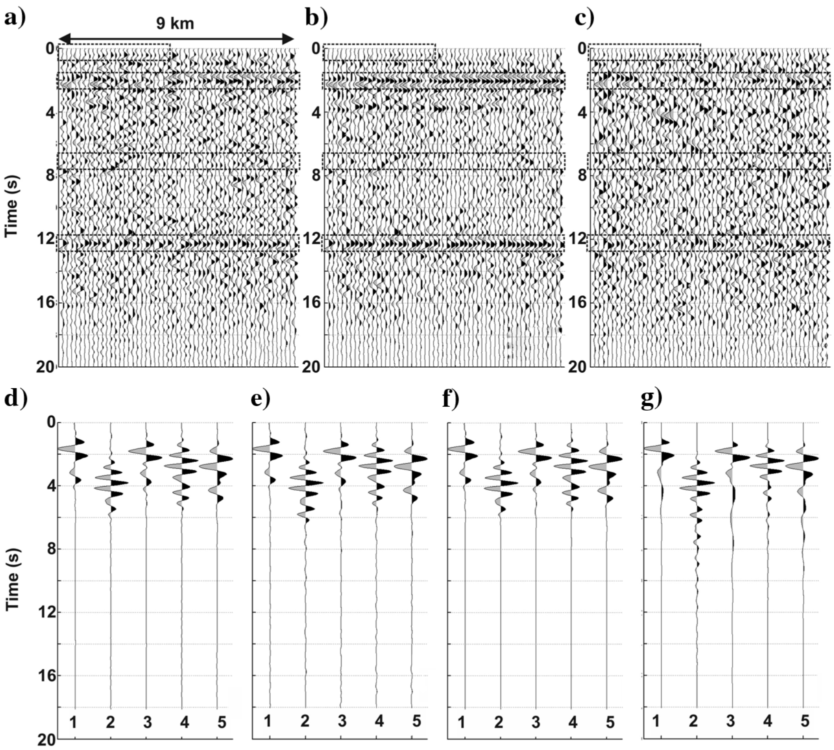

Figure 5. Estimated reflectivity time series and source wavelets from synthetic data with an S/N of 1: Reflectivity series (a) and source wavelets (d) from inversion without applying continuity constraints. Reflectivity series (b) and source wavelets (e) from inversion with enforced reflectivity constraints. (c) Reflectivity series obtained by deconvolution (reversed polarity). (f) Initial source wavelets for inversion and deconvolution. (g) True source wavelet used for generation of synthetic data. All traces are band-pass filtered in the range of 0.5–2.0 Hz.

section, the simplified model expressed by equation 1 does not take oblique incidence of the plane waves and receiver-side multiples into account. Thus, we perform a second suite of tests to address these issues. We also use a more complicated subsurface based on the SEG/EAGE salt model (Aminzadeh et al., 1996), of which we extract a 2D section. We extend the section down to a depth of 40 km with the Moho approximately at 33 km depth, and we further slightly modify the model to include more pronounced basement topography below the salt model. A shallow water layer is also included in the model. The compressional wave velocity below the basement starts at 6 km/s and increases with a vertical velocity gradient of 0.03 s^{-1}. The velocity below the Moho is 8.0 km/s. Density is calculated from V_P velocity by an empirical relationship given by Brocher (2005). For the salt body itself, we assume a constant density of 2 g/ccm. Acoustic modeling is performed using the CWP/SU: Seismic Un*x (Stockwell, 1999) acoustic finite-difference code sufdmod2. It should be noted that the methodology presented in this paper is also applicable to pressure data because the sign of the reflection coefficients for pressure is the same as for displacements. We use the same source wavelets as before, but their incidence angles below the Moho vary between −35° and +15°. The plane waves are simulated as line sources, with the source strength tapered toward the edges to suppress artifacts at the boundaries. The ocean surface is modeled as a free surface, and the modeled data include all the surface-related and internal multiples, which represent coherent noise within our linearized model approach (equation 1). Acoustic modeling does not take S-waves into account. However, the low velocities at the surface will bend the rays strongly toward the vertical, and hence the converted S-wave energy would be expected to be small. The blind deconvolution algorithm is applied for 100 receivers with a regular spacing of 135 m. The receivers are situated at 50 m depth, thus simulating hydrophones arranged along a streamer. White noise is added to the synthetic data, and preprocessing is limited to picking the first arrival and aligning the traces accordingly (Figure 6).

The reflectivity series from blind deconvolution and conventional deconvolution are shown in Figure 7, and in Figure 8b, we show a depth-converted reflectivity image of blind deconvolution. The blind deconvolution algorithm is applied with weak source wavelet weighting and continuity constraints, and it performs superior to conventional deconvolution. As in the previous tests, conventional deconvolution is more sensitive to random and coherent noise. The dominant features obtained from conventional deconvolution are multiples in the right side of the section, but not the basement topography. In contrast, blind deconvolution recovers the basement throughout the model, also below the salt model. There is no indication of the Moho, which should appear at approximately

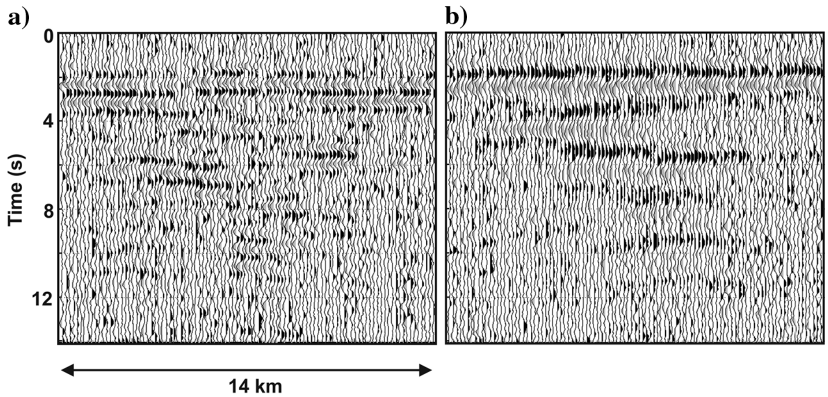

Figure 6. Synthetic data for the SEG/EAGE salt model. (a) Data for source wavelet 2 shown in Figure 3a. (b) Data for source wavelet 5 shown in Figure 3a.

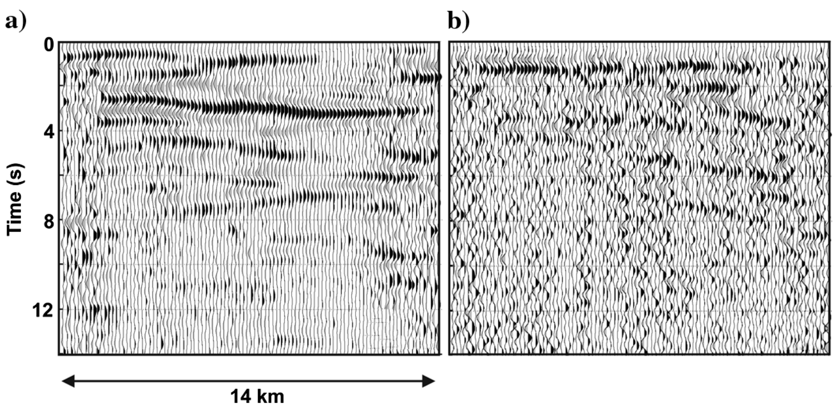

Figure 7. Reflectivity series obtained from blind deconvolution (a) and conventional deconvolution (b: reversed polarity). Conventional deconvolution enforces the higher-order multiples, in particular at the right side of the section.

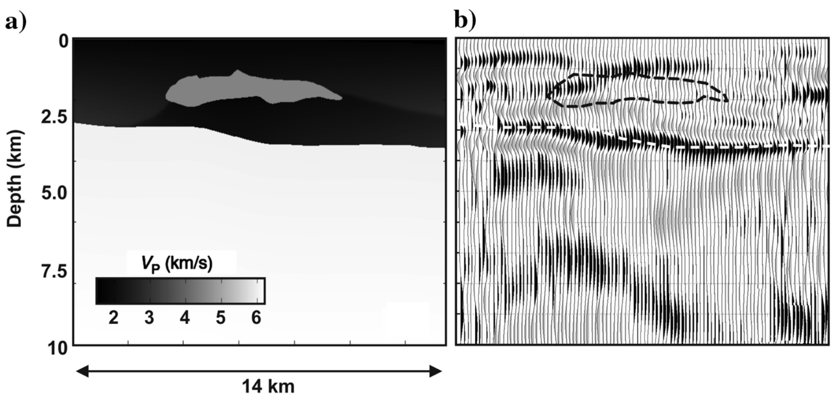

Figure 8. (a) The upper 10 km of the SEG/EAGE salt model section used for the synthetic test.(b) Depth-converted reflectivity series from blind deconvolution (Figure 7a). Conversion velocity is 2.25 km/s for depths down to 4 km and 6 km/s below. The dashed lines indicate the outline of the main structural features of the model section (a).

11 s two-way traveltime. This might be related to the varying incidence angles and the resulting destructive interference as discussed in the previous section. Also, for nonvertical incidence, the incidence point at the Moho is shifted with respect to the surface reflection point (Figure 1c). Thus, for a deep reflector, the vertical incidence assumption is more violated as for a shallow reflector. For the basement, the low velocities of the overburden bend the rays toward vertical incidence. Oblique incidence angles of teleseismic plane waves therefore have a lesser effect on imaging the basement. Above the basement, the top of the salt model might be interpreted. However, artifacts appear in the same time/depth range as the salt on both edges of the section such that this interpretation is not reliable without previous information on the subsurface structure. Those artifacts may be related to edge effects of the FD modeling algorithm and/or are possibly enforced by the imposed continuity constraints. An important conclusion from this test is that the subsalt structure is well recovered. We relate this to the low frequency and the plane wave characteristics of the seismic sources, which in sum results in less sensitivity to localized inhomogeneities in the subsurface structure. Also, the kink in the basement below the salt model is fairly well reconstructed, thus showing that nonflat structures can be imaged up to a certain extent.

APPLICATION TO FIELD DATA

The La Barge seismic experiment is an industry-academia cooperation and aims at evaluating the use of low-frequency passive seismic data for local subsurface characterization (Saltzer et al., 2011). From November 2008 to June 2009, 55 3C broadband instruments (Guralp CMG 3T, natural period 120 s) were continuously recording over an active oil/gas production site in Wyoming (Figure 9). The site is located in the La Barge region in the Green River Basin. On a local scale, the dominant structural feature is the low-angle Hogsback thrust, which separates claystones and siltstones in the east from an approximately 1-km-thick carbonate sequence in the west. The instruments were deployed at the surface with a very narrow station spacing of 250 m, and the sample interval was 10 ms. Data from the La Barge seismic experiment were subject to several other studies. Gans (2011) calculates P-to-S RFs for the entire crust and the uppermost mantle and finds remarkable variations on a very small spatial scale. Leahy et al. (2012) derive comparably high-resolution RF images of the shallow crust by exploiting the upper frequency range of teleseismic events. Byriol et al. (2013) retrieve velocity models of the shallow crust by finite-frequency traveltime inversion of regional seismic events. Behm et al. (2013) use traffic noise from a nearby road to obtain local surface wave velocities. Although all the applied methods have their origin in earthquake seismology, the novelty of most of these studies is their focus on the uppermost part of the crust (<5 km depth).

Teleseismic events

Due to the long recording interval, a large number of teleseismic events were collected. The assumption of vertical incidence implies the use of events with an epicentral distance greater than 25°, which in turn requires magnitudes greater than 5.5 for a clear observation. The strength of a particular teleseismic phase depends on the source mechanism and on the geologic structure at the source location. A well-defined wavelet may only be obtained if different phases of a single event, for example, direct arrival (P), reflection from the outer core (PcP), source-side surface reflection (pP), and midpoint surface reflection (PP), are well separated in time. The degree of separation depends on the distance and the depth of the event. Because some of these factors may be poorly known and/or weakly constrained, a visual inspection of a range of preselected event gathers is still necessary. The final selection criteria are the requirements of a short duration pulse of the source wavelet and the absence of later phases within a time range according to the investigation depth. We use direct arrivals (P) and source-side surface reflections (pP) of nine different events as source wavelets (Table 3). These wavelets have main frequencies between 0.4 and 1.2 Hz.

Data and preprocessing

Because this study focuses on P-waves, only vertical component data are used subsequently. The data are band-pass filtered between 0.6 and 4.0 Hz, and they are cut to a length of 30 s, starting 1 s prior to the earliest onset of the used phase (Figure 10, upper row). The traces are then aligned by their difference in arrival time to the receiver with the earliest onset. Arrival time picking is done manually. Correlation-based picking would provide higher accuracy, but the manual picking uncertainty (tens of ms) is sufficient still with respect to the targeted frequency range (0.5–2.0 Hz) of the inversion. The same accounts for the calculation of the initial source wavelet from the aligned traces. To avoid numerical issues in the inversion due to different magnitudes, all event gathers are normalized to their maximum amplitude.

An analysis of the entire data set suggests the presence of strong converted surface waves associated with most of the events (phase "cR" in Figure 10). Conversions from incident teleseismic body waves to Rayleigh waves are attributed to lateral Moho variations or rugged topography (e.g., Neele and Snieder, 1991). Their directionality indicates an origin in the west to northwest of the deployment, and their arrival times suggest conversion distances of and greater than 30 km. The southern part of the Wyoming Mountain Range is located in this area, and it is interpreted to account for the conversions, which occur as early as 6 s after the onset of the body waves. Because reflections from the lower crust and the Moho are expected to arrive between 8 and 14 s, the superposition of the converted surface waves poses an additional challenge. Singular value

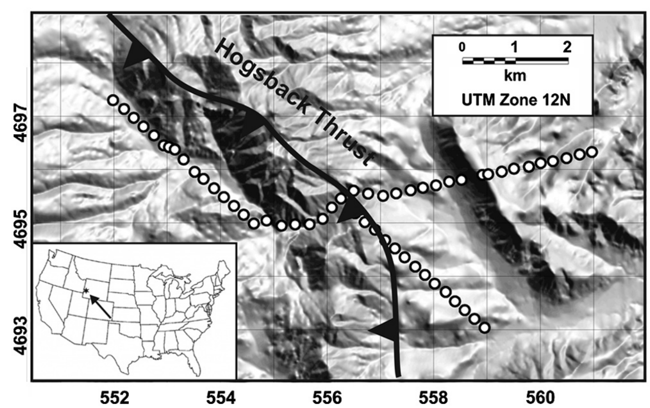

Figure 9. Location of the 55 broadband stations of the La Barge Passive Seismic Experiment. The Hogsback thrust separates carbonates in the west from claystones and siltstones in the east.

decomposition (SVD) of a wavefield is a practical way to attenuate or enforce laterally coherent features of event gathers (Freire and Ulrychs, 1988). By choosing a limited range of the largest singular values and corresponding singular vectors, laterally coherent signals are amplified at the expense of dipping phases and high-frequency noise. The choice of the range of singular values is somewhat subjective, and selecting too few singular values might result in suppressing laterally varying subsurface structures. Tests showed that in case of the P-phase, the inclusion of the upper 15% of the singular values and singular vectors provides a significant improvement of the inversion result without degrading the main structural features of the inverted reflectivity series. The corresponding number for the pP-phase is 40%.

Inversion

Inversions are carried out for P and pP data (Table 3), and the results are shown in Figure 11. Inversion parameters (Table 4) are partly chosen based on the insights from the synthetic tests. We further use conventional deconvolution as well as results from teleseismic traveltime inversion (Biryol et al., 2013) and RF analysis (Gans, 2011; Leahy et al., 2012) to validate our findings.

All inversions derive a continuous reflector with positive polarity at a time of approximately 2 s. The arrival times are slightly less in the western part. The results from the pP data (Figure 11c) are shifted by approximately 0.3 s compared to P data (Figure 11a). This shift might be related to the lower frequency of the pP wavelets and should be subject to further analysis. Enforcement of the continuity constraints (Figure 11b) facilitates the recovery of a reflector at approximately 14 s in the P data set. The result obtained from conventional deconvolution (Figure 11d) appears noisier overall, and consistent later arrivals are more difficult to interpret. The inversion from P data with continuity constraints (Figure 11b) is converted to depth with a 1D velocity depth-model based on the aforementioned studies (Figure 12). The shallow reflector at approximately 4 km depth correlates with the basement transition

Table 3. Used teleseismic events and phases for the application of blind deconvolution: P, direct arrival; pP, source-side surface reflection; and BAZ, receiver-event azimuth.

No.	Usage	Date/time location	Mag.	Distance (°)	BAZ (°)	Longitude (°)	Latitude (°)	Depth (km)
1	pP	2008-11-04/18:35:45 New Caledonia	6.3	95.0	251.7	168.46	−17.14	205
2	P, pP	2008-11-21/07:05:35 Solomon Islands	6.1	96.0	263.6	159.55	−8.95	263
3	pP	2009-03-15/08:19:05 Peru	5.7	67.4	137.6	−70.36	−14.45	189
4	pP	2009-03-20/12:26:03 Tonga	5.5	89.9	240.5	−179.38	−21.48	622
5	P	2009-04-18/02:03:53 Tonga	5.8	94.0	234.1	−177.45	−28.92	65
6	pP	2009-04-18/19:17:59 Kuril Islands	6.6	65.8	311.1	151.43	46.01	35
7	P	2009-04-21/05:26:12 Aleutian Islands	6.2	61.1	314.0	155.01	50.83	152
8	P	2009-05-22/00:24:21 Guatemala	5.5	33.1	143.4	−90.74	13.88	69
9	P	2009-05-22/19:24:19 Guatemala	5.6	26.2	153.8	−98.46	18.11	62

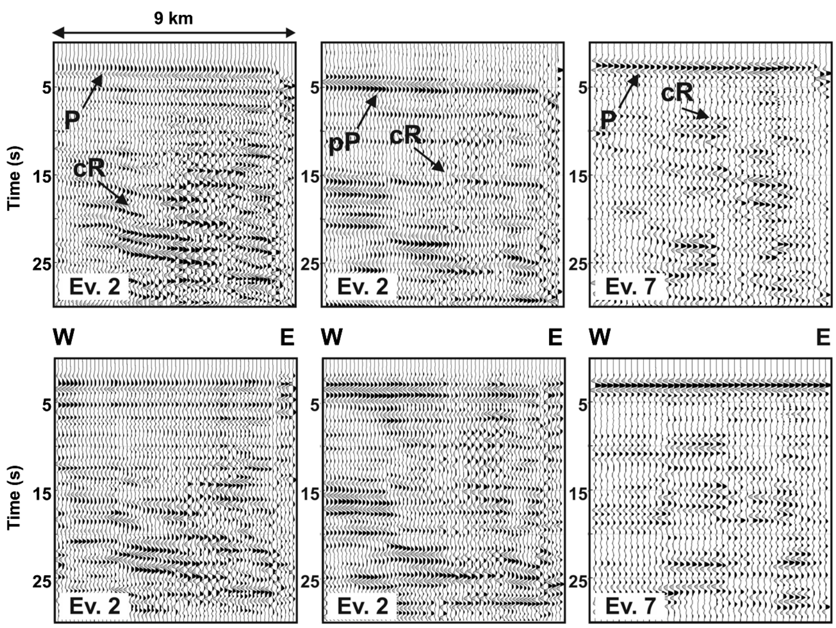

Figure 10. Examples of vertical component data used for the inversion (events 2 and 7, Table 3). P and pP refer to the teleseismic phases (P, direct arrival; pP, source-side surface reflection). Upper row: Band-pass filtered (0.6–4.0 Hz) event gathers. The time delay of the easternmost stations is due to their larger distances to the array. Note the converted surface waves (cR) arriving at times greater than 8 s. Lower row: Corresponding time-aligned and singular-value decomposed event gathers, which are the input data for inversion and deconvolution.

from low-velocity sandstones to high-velocity carbonates and granites. The small but significant apparent rise of the reflector in its western part is attributed to the uppermost thin sheet of carbonates prevailing only west of and above the low-angle Hogsback thrust. The higher velocities of the carbonates are not included in the 1D velocity model and result in an apparent shallower reflector in the depth-converted section. The Hogsback thrust itself cannot be deduced from the inversion, but a pronounced lateral change of the reflectivity is observed in the according depth range. Gans (2011) interprets a seismic discontinuity at ~15 km depth, but this is not indicated by the blind deconvolution inversion. The reason for this disagreement is not entirely clear, but it might be due to a combination of weak P-wave impedance contrast and superposition of converted surface waves in the data. Also, destructive interference of reflections from deeper structures might be taken into account. Although this applies for the Moho as well, the reflections from ~40 to 42 km depth correlate with the Moho depth range given by Gans (2011). The strong apparent dip (~8°) toward the west is surprising, but Gans (2011) also finds the Moho depths to be approximately 2 km deeper west of the Hogsback thrust than in the eastern part of the array. Considering the small array aperture, the enforced continuity constraints might smear an abrupt lateral change into a dipping structure. Lateral velocity changes above the Moho may also explain the apparent dip.

DISCUSSION

We start with comparing the presented inversion scheme to conventional deconvolution. The main difference is that the reflectivity series now is described by a model with which all observations must comply, whereas conventional (single-trace) deconvolution derives a new model for each seismic event. This drawback might be overcome by stacking deconvolved traces for several events, but there still is a strong sensitivity on noise. Modeling by inversion provides a more natural way to minimize the influence of white noise, although coherent noise over several traces (e.g., surface waves arriving at oblique angles or later arriving vertical-incidence waves) can be projected into the reflectivity model. The simultaneous estimation of the wavelet and the reflectivity series is considered as an advantage over methods that calculate the wavelet only prior to the reflectivity series. As with any inversion, constraints on the model and the determination (weights) of the unknowns can be incorporated in a flexible and natural way. The superposition with the source wavelet is an important modification to the conventional deconvolution model in

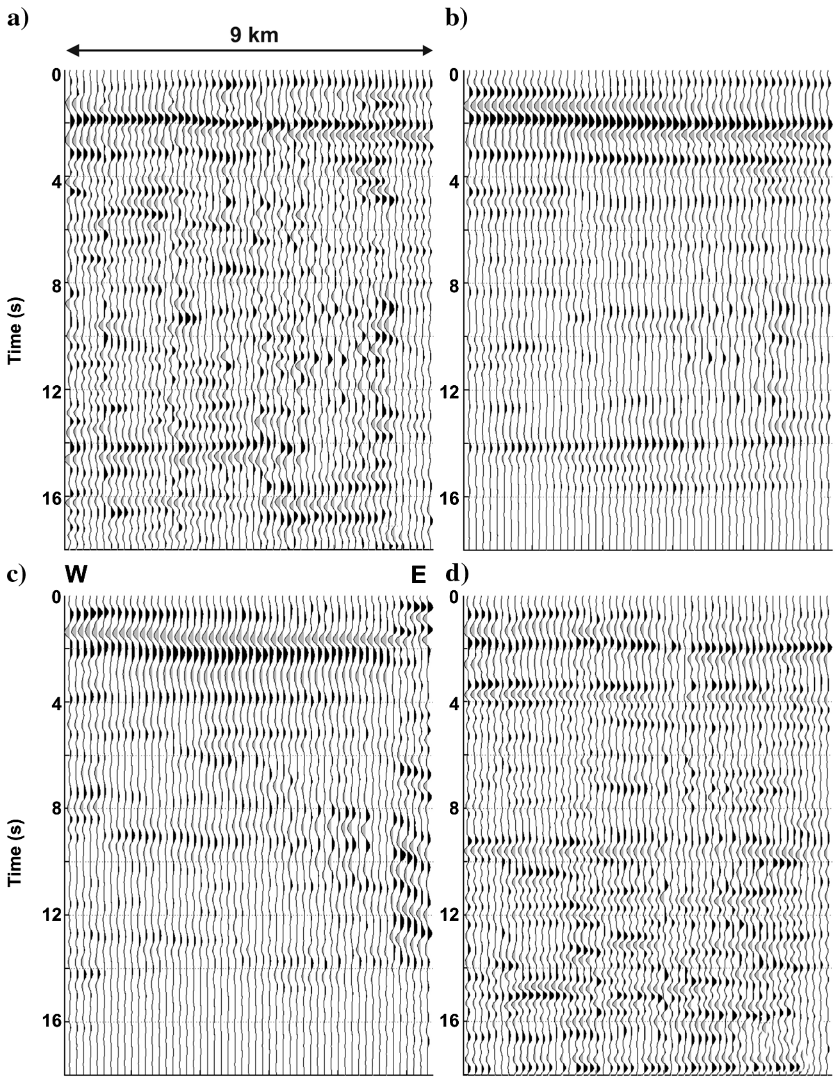

Figure 11. Reflectivity series obtained from the La Barge data. (a) Reflectivity series from P-phases without applying continuity constraints. (b) Reflectivity series from P-phases with enforced continuity constraints. (c) Reflectivity series from pP-phases without applying continuity constraints. (d) Conventional deconvolution of P-wavelets.The dashed gray line depicts the maximum amplitude of the shallow reflector in (b), and it is superimposed on the other panels for comparison.

Table 4. Parameter used for the inversion results shown in Figure 8. The SVD ratio α describes the threshold for singular values and vectors. Only those singular values, whose ratio to the largest singular value are higher than α, are used in for the inversion.

	Used phase/ number of events	SVD ratio α	Damping factor β/no. of iterations	Source weight	Initial source wavelet length (s)	Continuity constraints
Figure 11a	P/5	0.04	0.1/50	0.10	4.0	No
Figure 11b	P/5	0.002	0.1/50	0.15	4.0	Yes
Figure 11c	pP/5	0.15	0.1/50	0.10	5.3	No

case of shallow structures, in particular when the S/N is low (e.g., Figures 4 and 5). Application to synthetic and real data shows that the inversion scheme is more stable than conventional deconvolution. White noise is handled well by the inversion, but coherent noise over several traces presents a challenge, and such signals must be eliminated by preprocessing. If the cause of the coherent noise is known, it may also be modeled and estimated in the inversion. The assumption of vertical incidence presents a severe constraint to the method. In general, teleseismic events with epicentral distances greater than 25° and thus large magnitudes are required, and the need for clear and well-defined source wavelets imposes a strong selection criterion. In practice, it implies a long observation period to collect a sufficient number of events. In this study, the frequency range of the teleseismic phases is confined to 0.4 to 1.2 Hz, which limits the resolution capabilities. However, no special efforts were made to exploit the higher frequency range (5–10 Hz) of earthquake body waves (e.g., Leahy et al., 2012), and advanced preprocessing should also focus on this aspect in future studies. The assumption of a stationary source wavelet restricts the lateral extent of the deployment in general, but the actual aperture depends on the specific subsurface characteristics of a region in question. A laterally homogenous medium is more advantageous, and applications to other data sets will help to obtain a better understanding of the scale range of the method. The multichannel approach is not limited to a specific deployment geometry and thus is well suited for common passive seismic experiments on a local scale. Larger recording arrays may be targeted by allowing the source wavelet to vary spatially through interpolation, but this remains a subject for further study. The presented scheme can be used to supplement conventional RF methods due to the similar type of input data, but it does not require 3C observations. However, structural information on the shear-wave reflectivity might be additionally obtained by evaluating shear body waves on the horizontal components. With respect to the targeted depth range and resolution capabilities, low-frequency geophones with responses down to 1 Hz can be used in future deployments to substitute for costly broadband stations. The focus of the presented study is the inversion for local and shallow reflectivity series, and the inversion parameters are chosen in such a way as to derive a realistic subsurface model. This comes at the expense of projecting noise into the source wavelets. Future research should be dedicated to the applicability of the method for exact source wavelet reconstruction (e.g., by assuming realistic initial reflectivity models or advanced preprocessing). A potential improvement to the approach is to account for noncontinuous layering by convolving the right-hand side of equation 1 (excluding the noise) with an unknown transmission series at each station. At first glance, this would increase the number of unknowns and thus reducing the stability of the inversion. However, Claerbout (1968) shows how vertical reflection and transmission series are interdependent, and their relations can add additional constraints on the inversion. This may be useful for large station distances in which lateral continuity is not expected.

CONCLUSIONS

With respect to the initial question on the applicability for exploration seismology, the outlined method presents a potentially useful technique for local large-scale subsurface characterization from passive seismic data. Shallow to deep crustal structures can be imaged from a comparably low number of (well-suited) teleseismic earthquakes. As with any inversion technique, the results are sensitive to inversion parameters and the input data. Nonetheless, synthetic and real data examples indicate improved performance in comparison to conventional deconvolution, which is attributed to a common model for all observations. Synthetic tests suggest that the method and the used low-frequency sources provide improved large-scale imaging below local inhomogeneities (e.g., salt intrusion). Further studies, and in particular applications to other data sets, will help to develop a better understanding of the merits and practical limitations of the method.

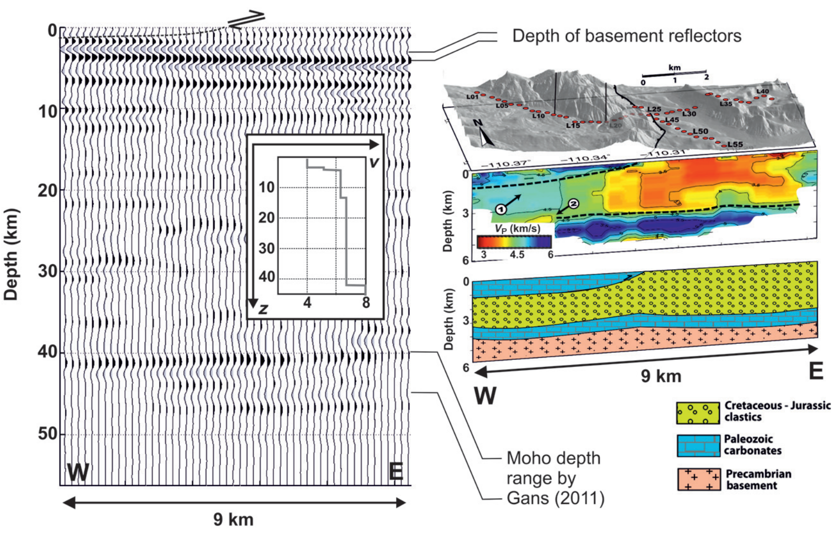

Figure 12. Depth converted seismic image from Figure 11b. The 1D velocity-depth model is based on previous studies (Gans, 2011; Leahy et al., 2012; Biryol et al., 2013). The cartoon including the geologic section and the velocity model is taken from Biryol et al. (2013). The dashed black line in the seismic image indicates the Hogsback thrust as known from surface geology and active source seismic investigations.

ACKNOWLEDGMENTS

We thank R. Snieder for discussion and helpful comments on the paper. B. Biryol kindly provided his cartoons for Figure 12. ExxonMobil funded this study. IRIS DMC was used to access the waveform data. SU stands for CWP/SU: Seismic Un*x, a processing line developed at Colorado School of Mines, partially based on the Stanford Exploration Project software. The comments of D. F. Halliday, C. Kostov, and two anonymous reviewers greatly improved the manuscript.

REFERENCES

Aki, K., and P. G. Richards, 2009, Quantitative seismology: University Science Books.

Aminzadeh, F., N. Burkhard, J. Long, T. Kunz, and P. Duclos, 1996, Three dimensional SEG/EAEG models — An update: The Leading Edge, **15**, 131–134, doi: 10.1190/1.1437283.

Bakulin, A., and R. Calvert, 2006, The virtual source method: Theory and case study: Geophysics, **71**, no. 4, SI139–SI150, doi: 10.1190/1.2216190.

Behm, M., R. Snieder, and G. M. Leahy, 2013, Retrieval of local surface wave velocities from traffic noise — An example from the La Barge basin (Wyoming): Geophysical Prospecting, **62**, 223–243, doi: 10.1111/1365-2478.12080.

Bensen, G. D., M. H. Ritzwoller, M. P. Barmin, A. L. Levshin, F. Lin, M. P. Moschetti, N. M. Shapiro, and A. Yang, 2007, Processing seismic ambient noise data to obtain reliable broad-band surface wave dispersion measurements: Geophysical Journal International, **169**, 1239–1260, doi: 10.1111/j.1365-246X.2007.03374.x.

Biryol, C. B., G. M. Leahy, G. Zandt, and S. L. Beck, 2013, Imaging the shallow crust with local and regional earthquake tomography: Journal of Geophysical Research, **118**, 2289–2306, doi: 10.1002/jgrb.50115.

Bostock, M. G., 2004, Green's functions, source signatures, and the normalization of teleseismic wave fields: Journal of Geophysical Research, **109**, B03303, doi: 10.1029/2003JB002783.

Bostock, M. G., and M. D. Sacchi, 1997, Deconvolution of teleseismic recordings for mantle structure: Geophysical Journal International, **129**, 143–152, doi: 10.1111/j.1365-246X.1997.tb00943.x.

Brocher, T., 2005, Empirical relation between elastic wavespeeds and density in the earth's crust: Bulletin of the Seismological Society of America, **95**, 2081–2092, doi: 10.1785/0120050077.

Cadzow, J. A., and X. Li, 1995, Blind deconvolution: Digital Signal Processing, **5**, 3–20, doi: 10.1006/dspr.1995.1002.

Claerbout, J., 1968, Synthesis of a layered medium from its acoustic transmission response: Geophysics, **33**, 264–269, doi: 10.1190/1.1439927.

Denes, V., E. Starr, and J. Kapoor, 2009, Developing Earth models with full waveform inversion: The Leading Edge, **28**, 432–435, doi: 10.1190/1.3112760.

Draganov, D., X. Campman, J. Thorbecke, A. Verdel, and K. Wapenaar, 2009, Reflection images from ambient seismic noise: Geophysics, **74**, no. 5, A63–A67.

Edme, P., and D. F. Halliday, 2012, Near-surface imaging from point-receiver ambient noise: 74th Annual International Conference and Exhibition, EAGE, Extended Abstracts, X007.

Forghani, F., and R. Snieder, 2010, Underestimation of body waves and feasibility of surface-wave reconstruction by seismic interferometry: The Leading Edge, **29**, 790–794, doi: 10.1190/1.3462779.

Freire, S. L. M., and T. J. Ulrychs, 1988, Application of singular value decomposition to vertical seismic profiling: Geophysics, **53**, 778–785, doi: 10.1190/1.1442513.

Galetti, E., and A. Curtis, 2012, Generalised receiver functions and seismic interferometry: Tectonophysics, **532**, 1–26, doi: 10.1016/j.tecto.2011.12.004.

Gans, C. R., 2011, Investigations of the crust and upper mantle of modern and ancient subduction zones, using Pn tomography and seismic receiver functions: Ph.D. thesis, University of Arizona.

Gurrola, H., G. E. Baker, and J. B. Minster, 1995, Simultaneous time-domain deconvolution with application to the computation of receiver functions: Geophysical Journal International, **120**, 537–543, doi: 10.1111/j.1365-246X.1995.tb01837.x.

Kaaresen, K. F., and T. Taxt, 1998, Multichannel blind deconvolution of seismic signals: Geophysics, **63**, 2093–2107, doi: 10.1190/1.1444503.

Leahy, G. M., R. L. Saltzer, and J. Schmedes, 2012, Imaging the shallow crust with teleseismic receiver functions: Geophysical Journal International, **191**, 627–636, doi: 10.1111/j.1365-246X.2012.05615.x.

Neele, F., and R. Snieder, 1991, Are long-period body wave coda caused by lateral heterogeneity?: Geophysical Journal International, **107**, 131–153, doi: 10.1111/j.1365-246X.1991.tb01162.x.

Otis, R., and R. Smith, 1977, Homomorphic deconvolution by log spectral averaging: Geophysics, **42**, 1146–1157, doi: 10.1190/1.1440780.

Rawlinson, N., and M. Sambridge, 1998, Seismic travel time tomography of the crust and lithosphere: Advances in Geophysics, **46**, 81–198, doi: 10.1016/S0065-2687(03)46002-0.

Ruigrok, E., X. Campman, D. Draganov, and K. Wapenaar, 2010, High-resolution lithospheric imaging with seismic interferometry: Geophysical Journal International, **183**, 339–357, doi: 10.1111/j.1365-246X.2010.04724.x.

Ryan, H., 1994, A choice of wavelets: CSEG Recorder, **9**, 24–25.

Saltzer, R., G. M. Leahy, J. Schmedes, J. Roth, and E. Rumpfhuber, 2011, Earthquakes – A naturally occurring source of low frequency data: 81st Annual International Meeting, SEG, Expanded Abstracts, 3689–3693.

Schuster, G. T., 2010, Seismic interferometry: Cambridge University Press.

Sirgue, L., and R. Pratt, 2004, Efficient waveform inversion and imaging: A strategy for selecting temporal frequencies: Geophysics, **69**, 231–248, doi: 10.1190/1.1649391.

Snieder, R., 2004, Extracting the Green's function from the correlation of coda waves: A derivation based on stationary phase: Physical Review E, **69**, 046610, doi: 10.1103/PhysRevE.69.046610.

Stockwell, J. W., Jr., 1999, The CWP/SU: Seismic Un*x Package: Computers & Geosciences, **25**, 415–419, doi: 10.1016/S0098-3004(98)00145-9.

Tria, M., M. Van Der Baan, A. Larue, and J. W. Mars, 2007, Wavelet estimation and blind deconvolution of realistic synthetic seismic data by log spectral averaging: 77th Annual International Meeting, SEG, Expanded Abstracts, 1982–1986.

Tseng, T.-L., and W.-P. Chen, 2006, Probing the Southern Indian shield with P-wave receiver-function profiles: Bulletin of the Seismological Society of America, **96**, 328–333, doi: 10.1785/0120050074.

van der Baan, M., and D.-T. Pham, 2008, Robust wavelet estimation and blind deconvolution of noisy surface seismic: Geophysics, **73**, no. 5, V37–V46, doi: 10.1190/1.2965028.

Wapenaar, K., D. Draganov, R. Snieder, X. Campman, and A. Verdel, 2010, Tutorial on seismic interferometry: Part 1 — Basic principles and applications: Geophysics, **75**, no. 5, A195–A209, doi: 10.1190/1.3457445.

Wiggins, R., 1978, Minimum entropy deconvolution: Geoexploration, **16**, 21–35, doi: 10.1016/0016-7142(78)90005-4.

Yang, Z., A. F. Sheehan, W. L. Yeck, K. C. Miller, E. A. Erslev, L. L. Worthington, and S. H. Harder, 2012, Imaging basin structure with teleseismic virtual source reflection profiles: Geophysical Research Letters, **39**, L02303, doi: 10.1029/2011GL050035.